Transmission electron microscopy and first-principles calculations of hydrogen ordering in β-YH_{2+x}

L. A. Bendersky, B. Burton, and K. Wang
Materials Science and Engineering Laboratory, National Institute of Standards and Technology, Gaithersburg, Maryland 20899, USA
(Received 24 May 2010; revised manuscript received 20 July 2010; published 20 October 2010)

In YH_{2+x} hydrides stoichiometric deviations are associated with various interesting phenomena such as magnetic transitions and metal-insulator transitions; ordering of hydrogen on the octahedral sites (O sites) was suggested to be responsible. Long-range order was discovered in hydrogenated Y films by electron diffraction and high-resolution transmission electron microscopy. Ordering on interstitial O sites in the fcc-based $Y_{fcc}H_{2+x}$ solid solution ($0<x<1$) was investigated with computational tools from the Alloy Theoretic Automated Toolkit. The resulting set of 94 structure energies was fit to a cluster-expansion Hamiltonian that was used to perform a ground-state analysis for the mostly metastable fcc-based solid solution and for the more stable $Y_{fcc}H_{2+x}+Y_{hcp}H_{2+x}$ two-phase mixture. The calculated structures were tested by the observed diffraction conditions and two possible ordered structures were suggested, a ground-state triclinic $x=0.0625$ and an I-centered cubic $x=0.375$.

DOI: 10.1103/PhysRevB.82.144111 PACS number(s): 68.37.Lp

I. INTRODUCTION

There is considerable interest in the hydrogenation process of rare-earth (R) elemental metals and particularly thin films, owing to the rich variety of physical phenomena that they exhibit: (1) a decrease in the carrier density with increasing hydrogen content, which gives rise to a metal-to-insulator transition; (2) optical changes from reflecting to a transparent state; (3) an array of magnetic states and magnetic ordering transitions in R-H, when R is a magnetic ion.[1–3] These phenomena are related to the formation of ordered hydride phases, and the optical changes may enable technological exploitation as switchable mirrors.[4,5]

Rare-earth metals readily absorb hydrogen and typically form three hydride phases: (1) a solid solution based on an hcp substructure of R atoms (α-hcp phase, $P6_3/mcm$, with up to 35 at. % H at higher temperatures, e.g., for Y or Sc); (2) a CaF_2-structure RH_2 dihydride phase with an fcc R-atom substructure and, ideally, H atoms filling the tetrahedral interstices; and (3) a trihydride RH_3 with an hcp-based R-atom substructure ($P\bar{3}c1$).[1,2,6–8]

The prototypical R-H phase diagram (e.g., for R=Y, Nd, Sm, and Ho, but more complicated for La or Pr) has relatively broad hydrogen solubility ranges for its α-hcp, $R_{fcc}H_2$, and $R_{hcp}H_3$ phases that are separated by α-hcp+$R_{fcc}H_2$ and $R_{fcc}H_2+R_{hcp}H_3$ two-phase fields,[1,2] which give rise to plateaus in ($\log_{10} P_H$ vs H/R ratio) hydrogenation plots. Accordingly, hydrogen charging of R-H systems yields the sequential formation of α-hcp, $R_{fcc}H_2$, and $R_{hcp}H_3$ phases with increasing H content. These phases have been studied by a variety of methods including neutron scattering[6,7,9] in both hydrides and deuterides for R=Y, Nd, Tb, Dy, Ho, Er, Tm, and Lu,[6–8] optical transmission,[4,5,10] electrical and magnetic measurements,[1–3,11] electrochemical charging,[12] Raman spectroscopy,[13,14] x-ray diffraction (XRD),[15] infrared imaging,[16] and transmission electron microscopy (TEM).[17–20] Stabilities of many $R_{fcc}H_{2+x}$ ($0>x>1$) phases have also been investigated by first-principles calculations.[21–25]

Typically, the R hydride/deuteride phases have wide homogeneity ranges around their ideal stoichiometries, and these stoichiometric deviations are associated with various interesting phenomena such as magnetic transitions, metal-insulator transitions, and H ordering, particularly in the $R_{fcc}H_{2+x}$ phases.[1–3] Ideally, stoichiometric $R_{fcc}H_2$ has the CaF_2 fluorite structure with all tetrahedral sites (T sites) occupied by H. In the composition range RH_2-RH_3, H atoms in $R_{fcc}H_{2+x}$ solid solutions must occupy both T sites and octahedral interstitial sites (O sites), and if all T and O sites are filled the stoichiometry is RH_3. Thus, one expects the low-temperature phase equilibria of $R_{fcc}H_{2+x}$ solid solutions (stable or metastable) to be characterized by hydrogen ordering on the O sites and this is the principal focus of this paper.

The maximum value of x at which a $R_{fcc}H_{2+x}$ phase is (meta)stable relative to an $R_{fcc}H_2+R_{hcp}H_3$ two-phase mixture depends on the R atom: experimentally, the maximum (meta)stable value for x approaches 0 for heavy R elements (e.g., Lu) and approaches 1 when R is a light R element (e.g., La or Ce), with x for all other R's in between (with the exception of Sc).[3,26]

In a first-principles study of coherent (mostly metastable) YH_{2+x} phase stability[21] a cluster-expansion (CE) Hamiltonian[27,28] was fit to structure energies for $Y_{fcc}H_2$ and $Y_{fcc}H_3$ and nine intermediate O-site-ordered superstructures. Relative to the fcc-based end members, the formation energies, ΔE_f, for fcc-based DO_{22}, "40," and $D1_a$ superstructures (at $x=0.25$, 0.5, and 0.8, respectively) are all negative and lie on the convex hull. Thus, the DO_{22}, 40, and $D1_a$ superstructures were predicted as fcc-based ground states (GSs) for the small number of structures that was considered; note, however, that $Y_{fcc}H_{2+x}$ stability with respect to $Y_{hcp}H_3$ was not considered.

The CE Hamiltonian was also used in a cluster-variation method calculation[28] of an fcc-based coherent phase diagram in the range $0<x<0.6$; the calculated diagram has stability fields for the following structures: a disordered $Y_{fcc}H_{2+x}$ phase and two ordered phases, DO_{22} with a broad homogeneity range and a 40.[21] The calculated second-order order-disorder transition temperature at $x=0.1$ for the DO_{22} structure is around 280 K, which is similar to the observation of a

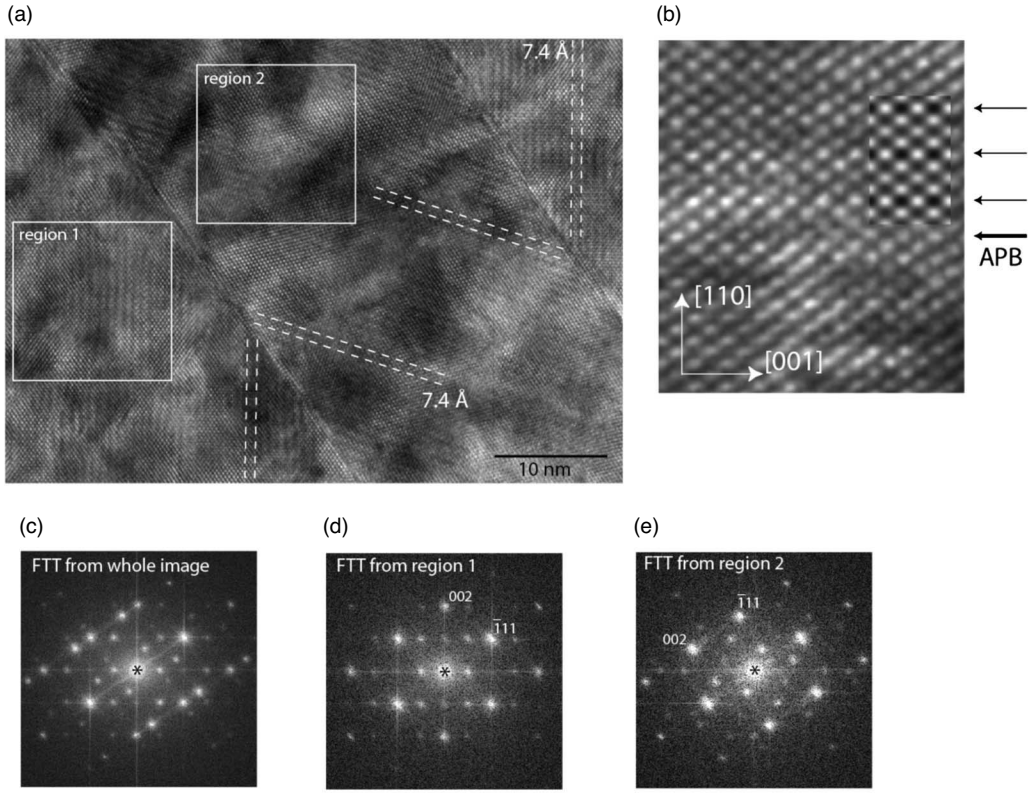

FIG. 1. (a) HRTEM image of alternating twin lamellae of YH_2, both in a [110]-zone axis orientation. The lamellae are separated by near-edge-on (111) oriented interfaces. (b) Enlargement of the HRTEM image showing a phase contrast of an fcc arrangement of Y. Intensity modulations due to ordering are indicated with arrows. The inset is from the simulations of phase contrast for the I-centered relaxed structure. (c)–(e) Fast Fourier transform patterns from a large area which includes (c) both variants and (d) and (e) from individual variants showing the presence of $k_1=1/4[220]^*$ and $k_2=1/2[002]^*$ superlattice reflections.

metal-semiconductor transition near 230–280 K and resistivity anomalies near 200–250 K for the system with x near 0.1.[26] No ordered $Y_{fcc}H_{2+x}$ phase was observed in structural investigations, however, neutron scattering (vibrational spectroscopy and powder diffraction) indicated a short-range order arrangement akin to the long-range order of hypothetical $Y_{fcc}H_{2.25}$ $I4/mmm$ structure.[8] However the DO_{22}-type ordered phase has been reported in some other $R_{fcc}H_{2+x}$ systems: e.g., CeH_{2+x} and TbD_{2+x}.[29,30] The DO_{22}-type ordered phase has tetragonal O-site ordering, analogous to the ordering of Ti in Al_3Ti; as far as we know, the DO_{22} type is the only $R_{fcc}H_{2+x}$ derived long-range O-site-ordered structure that has been reported. We did not calculate an fcc-based coherent phase diagram, but it is clear from the GS results presented below that if we had, it would be very different from the previously calculated diagram.

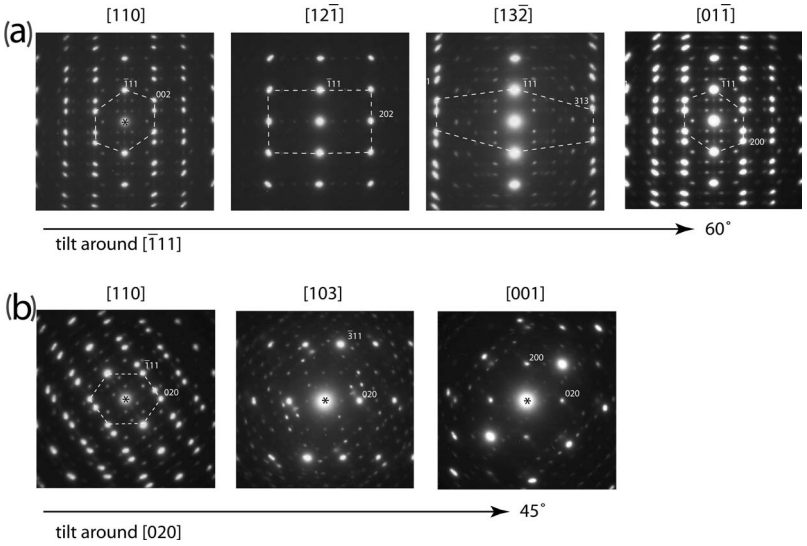

FIG. 2. SAED patterns obtained by tilting the same sample regions around (a) $[\underline{1}11]^*$ and (b) $[002]^*$ reciprocal space directions. Dashed lines outline a cell of one variant. The patterns are indexed with the YH2 fcc lattice.

TABLE I. Atomic coordinates of an idealized I-centered structure, $a=2a_{YH_2}=1.04$ nm and space group. The coordinates were later refined by energy minimization calculations.

Atom	Wyckoff site xyz	Free positional parameters
Y_1	$2A$: 0 0 0	
Y_2	$6b$: $\frac{1}{2}, \frac{1}{2}, \frac{1}{2}$	
Y_3	$24h$: $0,y,y$	$y\sim 1/4$
H_{T1}	$16f$: x,x,x	$x\sim 1/8$
H_{T2}	$48k$: x,x,z	$x\sim 1/8$; $z\sim 3/8$
H_O	$12e$: $x,0,0$	$x\sim 1/4$

Recently, we investigated formation of hydride phases in near-epitaxial Y films by various methods including TEM,[16,20] and our electron-diffraction data indicate that the $Y_{fcc}H_{2+x}$ phase exhibits long-range O-site order. Although there have been previous TEM (Refs. 17–19) and XRD (Refs. 31 and 32) studies of hydrogenated Y films, we found no reports of O-site ordering in $Y_{fcc}H_{2+x}$ films. Examination of the diffraction-based reciprocal space indicates that O-site ordering occurs, but it is not of the DO_{22} type. It is best described by an I-centered Y_{16} cell ($a=2a_{YH_2}=1.04$ nm) in which, ideally, all T sites and 12 of the 32 O sites are occupied by hydrogen, or by a triclinic structure of the composition $YH_{2+1/16}$.

II. EXPERIMENTAL PROCEDURES

Y films were prepared by electron-beam evaporation on (0001)-Al_2O_3 substrates covered with a Ti buffer layer and were then hydrogenated for different times (see Ref. 12 for experimental details). The structure that is discussed here was observed in films that were hydrogenated for 10 min at 523 K under 0.490 MPa of ultrahigh-purity hydrogen gas; x-ray diffraction and TEM indicate that it is a [111]-oriented $Y_{fcc}H_{2+x}$ phase.

Cross-sectional thin foils for TEM observations were prepared by cutting, mechanically thinning (grinding and dimpling), and Ar-ion milling at liquid-nitrogen temperature. After ion milling, the TEM specimens were immediately transported into the TEM for observation. To reduce the damage from electron-beam irradiation during TEM observation, focusing and diffraction operations were carried out on a part of the TEM specimen with direct imaging accomplished by moving to a fresh part of the sample.

III. SUMMARY OF EXPERIMENTAL OBSERVATIONS

As described in our previous paper,[20] the Y films were grown with the following orientation relationship: $(0001)[11\bar{2}0]_Y \| (0001)[11\bar{2}0]_{Ti} \| (0001)[10\bar{1}0]_{Al_2O_3}$. Hydrogenation of the hcp Y films transforms them to the $Y_{fcc}H_{2+x}$ phase, yielding two twin-related orientational variants with [111] normal to the substrate. This orientation relationship results from reshuffling of close-packed planes from hcp stacking, *A-B-A-B-*, to fcc stacking, *A-B-C-A-B-C-*.

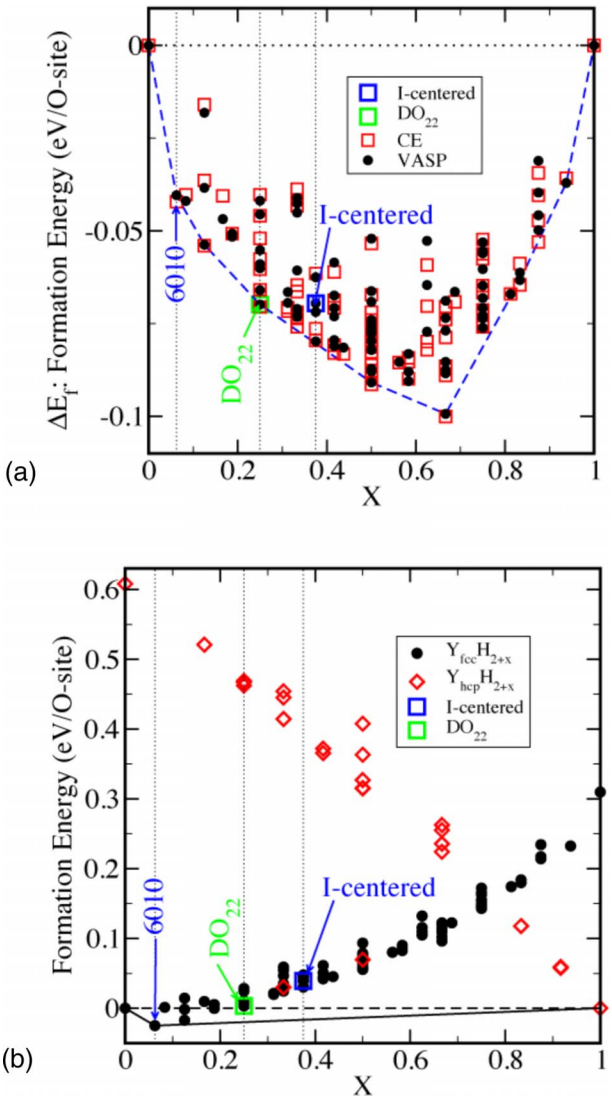

FIG. 3. (Color online) (a) Ground states of the fcc-based $Y_{fcc}H_{2+x}$ ($0<x<1$) subsystem: solid circles are formation energies, relative to $Y_{fcc}H_2$ and $Y_{fcc}H_3$ reference states, which were calculated from first principles (VASP code); open squares (CE, red) are formation energies that were calculated with a cluster-expansion Hamiltonian; formation energies for the DO_{22} and I-centered structures are plotted as large filled squares (green and blue, respectively); the dashed line (blue) is the fcc-based convex hull. (b) Comparison of the first-principles results for fcc-based $Y_{fcc}H_{2+x}$ (solid circles) and hcp-based $Y_{hcp}H_{2+x}$ formation energies (open diamonds, red). Other symbols are as in (a) except that here the convex hull is plotted as a solid black line.

Examination of the twin structure by high-resolution TEM (HRTEM) imaging and selected area electron diffraction (SAED) reveals the superstructure of $Y_{fcc}H_{2+x}$. Figure 1(a) shows a phase-contrast HRTEM image of alternating twin lamellae separated by near-edge-on (111) oriented interfaces both in the $\langle 110\rangle_{YH_2}$ zone axis. The image shows an arrangement of bright spots that is typical for a [110] oriented fcc structure [Fig. 1(b)]; however, the intensities of spots are modulated into a set of 0.74-nm-wide fringes running parallel to (002) planes [Fig. 1(a)]. The modulation contributes a

TABLE II. Types of the SAED patterns for the ⟨100⟩ and ⟨110⟩ orientations of an fcc-Y sublattice according to the diffraction simulations of different ground-state structures. Diffraction zone axes of the structures are given in the indices of a corresponding lattice. Differences in superlattice reflections (both positions and intensities) are indicated by letters A–D and I. The relationships between the YH_2 fcc lattice and the Bravais lattices of the structures are presented.

YH_{2+x} structures	x	Diffraction zone axes		Bravais lattices and relations to fcc-YH_2
		⟨001⟩ fcc type	⟨011⟩ fcc type	
8106 relaxed	0.0625	[001] (I)	[110] (I)	Tetragonal $2\times2\times1$
		[010] (A)	[012] (A)	
		[100] (A)	[102] (A)	
6010 relaxed	0.0625	[011] (I)	[112] (I)	Triclinic
		[101] (I)	[121] (I)	
		[110] (I)	[211] (I)	
			[01$\bar{1}$] (I)	
			[10$\bar{1}$] (I)	
			[$\bar{1}$10] (I)	
8105	0.125	[001] (I)	[$\bar{1}$10] (A)	Tetragonal $2\times2\times1$
		[010] (A)	[012] (A)	
		[100] (I)	[110] (A)	
DO_{22} relaxed	0.25	[001] (A)	[021] (A)	Tetragonal $1\times1\times2$
		⟨010⟩ B	[201] (A)	
			[110] (A)	
3531	0.375	[001] (I)	⟨010⟩ (I)	Tetragonal $\sqrt{2}\times\sqrt{2}\times2$
		⟨010⟩ (B)	⟨111]⟩ (A)	
I-centered relaxed	0.375	⟨100⟩ (I)	⟨110⟩ (I)	Cubic $2\times2\times2$
3383	0.5	⟨110⟩ (B)	[010] (I)	Tetragonal $\sqrt{2}\times\sqrt{2}\times2$
		[001] (C)	[$\bar{1}$11] (A)	
			[100] (A)	
			[11$\bar{1}$] (A)	
323	0.6667	[001] (D)	[21$\bar{3}$] (A)	Monoclinic $\sqrt{5}\times\sqrt{5}\times1$
		[120] (A)	[100] (I)	
		[210] (A)	[123] (A)	

set of weak reflections $\frac{1}{2}(002h)$ and $\frac{1}{4}(\bar{2}\bar{h}2h0)$ evident in fast Fourier transforms of the HRTEM image in Figs. 1(c)–1(e). The same superlattice reflections were clearly observed in SAED patterns. The commensurate nature of the reflections suggests that the superstructure is based on O-site ordering in $Y_{fcc}H_{2+x}$.

For completeness, a series of tilting experiments were conducted to obtain positions of superlattice reflections in a three-dimensional reciprocal lattice. Figures 2(a) and 2(b) show two sequences of major SAED patterns acquired during tilting around $[111]_{fcc}$ and $[002]_{fcc}$ directions of one of the twin variants. Because the twin lamellae are very small, the SAED patterns include reflections belonging to both variants. Tilting of the [110] pattern 60° around $[111]_{fcc}$ results in the equivalent [101] pattern and tilting 45° around $[002]_{fcc}$ results in the [001] pattern. Summary of the tilting experiments shows that the positions of the superlattice reflections preserve cubic symmetry. Assuming that the cubic substructure is not distorted, in our recent work we suggested an idealized structural model with an I-centered cubic $a=2a_{YH_2}=1.04$ nm Bravais lattice and space group $Im\bar{3}m$ (Ref. 20); the structure is described in Table I. An ideal stoichiometry of the structure is $Y_{fcc}H_{2+3/8}$.

IV. COMPUTATIONAL PROCEDURE

Interstitial O-site H:O ordering in the fcc-based $Y_{fcc}H_{2+x}$ solid solution $(0<x<1)$ was investigated with computational tools from the Alloy Theoretic Automated Toolkit.[33–35] We performed total-energy calculations for 93 $Y_{fcc}H_{2+x}$ supercells with different H:O configurations on the O sites, with all T sites fully occupied by H. The resulting set of 94 structure energies, $\{E_{str}\}$, was fit to a CE Hamiltonian that was used to perform a GS analysis for the mostly metastable fcc-based solid solution and for the more stable $Y_{fcc}H_{2+x}+Y_{hcp}H_{2+x}$ two-phase mixture.

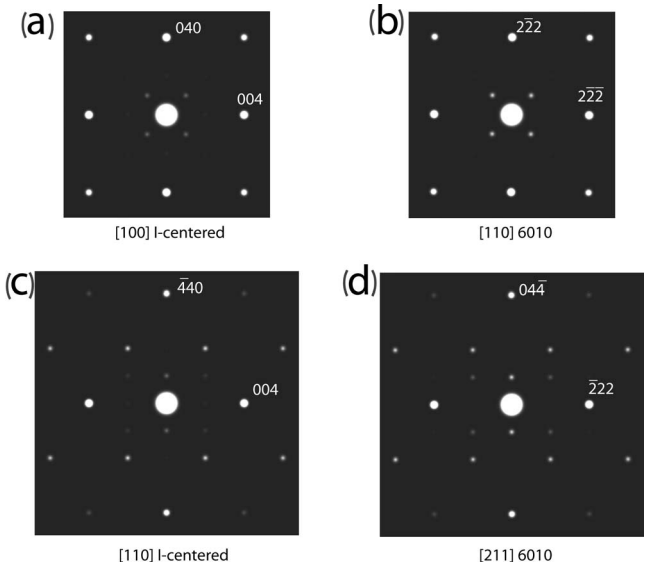

FIG. 4. Calculated electron-diffraction patterns of the (a) and (c) I-centered and (b) and (d) 6010 relaxed structures at (a) and (b) ⟨100⟩-type and (c) and (d) ⟨011⟩-type zone axes. All calculations are kinematic, with fixed crystal thickness of 50 nm and a level of intensities.

V. TOTAL ENERGY CALCULATIONS

All total-energy calculations were performed with the Vienna *ab initio* simulation program[36–40] (VASP, version 445) using projector augmented wave pseudopotentials, with the generalized gradient approximation for exchange and correlation energies. Electronic degrees of freedom were optimized with a conjugate gradient algorithm. Both cell constant and atomic positions were fully relaxed without symmetry constraints. Pseudopotential valence electron configurations were H, $1s^1$; Y_{pv}, $4s^2 4p^6 5s^2 4d$. Total energies were calculated for $Y_{fcc}H_2$, $Y_{fcc}H_3$, and 92 fcc-$Y_{fcc}H_{2+x}$ superstructures where $0<x<1$.

Total energy calculations were converged with respect to *k*-point meshes by using the equivalent of $6\times6\times6$ or greater for an fcc cell with four Y atoms. A 500 eV energy cutoff was used in the "high-precision" option that yields *absolute* energies converged to within a few meV per O site (a few tenths of a kilojoule per O site). Residual forces were typically on the order of 0.02 eV or less.

To test the hypothesis that O-site ordering can be treated separately from T-site ordering, i.e., the approximation that all T sites are occupied by H, a series of 60 structure energies was calculated for superstructures with various hydrogen configurations on both T and O sites. These calculations confirmed the strong T-site preference of H, suggesting that the separate treatment of O-site ordering is justified.

In addition, structure energy calculations were performed for $Y_{hcp}H_3$, $Y_{hcp}H_2$, and 32 $Y_{hcp}H_{2+x}$ ordered structures to address the question of O-site vacancy solubility in $Y_{hcp}H_3$, i.e., is the stable $Y_{hcp}H_{2+x}$ phase in equilibrium with the fcc-based solid solution essentially stoichiometric $Y_{hcp}H_3$ or is there significant O-site vacancy solubility toward $Y_{hcp}H_2$?

Results of these calculations are plotted in Figs. 3(a) and 3(b). Figure 3(a) is a plot of the fcc-based $Y_{fcc}H_{2+x}$ subsystem (ΔE_f, defined relative to $Y_{fcc}H_2$ and $Y_{fcc}H_3$) in which solid circles indicate the 94 ΔE_f for $Y_{fcc}H_{2+x}$ VASP calculations, open squares (red) indicate the corresponding CE values, larger open squares indicate VASP calculations of ΔE_f for the DO_{22} structure (green, $x=0.25$), and the I-centered structure [blue, $x=0.375$ (Ref. 41)]. The dashed line (blue) is the convex hull, which indicates mostly metastable fcc-based GS. Seven ordered fcc-subsystem GSs are predicted, including the DO_{22} structure, but not the I-centered structure. Because the DO_{22} and I-centered structures are of high symmetry, T-dependent (Refs. 36–40) calculations were performed prior to final 0 K structure energy minimization: for DO_{22} this yielded no significant change in ΔE_f, i.e., change <0.01 meV/O site; for the I-centered phase it yielded an ~0.7 meV/O-site reduction in ΔE_f. The latter is marginally significant and includes a possible symmetry reduction that was determined with the FINDSYM (Ref. 41) program; i.e., within a tolerance factors (in angstroms) of $t=0.01$, 0.001, 0.0001, and 0.000 01 space-group symmetries are calculated as $Im\bar{3}m$, $R\bar{3}m$, $C2/m$, and $C1$, respectively.

In Fig. 3(b), the ΔE_f's are defined relative to reference states $Y_{fcc}H_2$ and $Y_{hcp}H_3$. Symbols are the same as in Fig. 3(a) except that here open diamonds (red) indicate the ΔE_f for $Y_{hcp}H_{2+x'}$; note that three $Y_{hcp}H_{2+x}$ structures have formation energies that are similar to those for $Y_{fcc}H_{2+x}$ (two structures at $x=1/3$ have almost identical energies and therefore plot as if they were only one). The solid black lines indicate the (stable) convex hull: only one $Y_{fcc}H_{2+x}$-ordered structure at $x=0.0625$ (labeled as 6010 in Fig. 3) is predicted to be stable relative to a $Y_{fcc}H_2+Y_{hcp}H_3$ two-phase mixture.

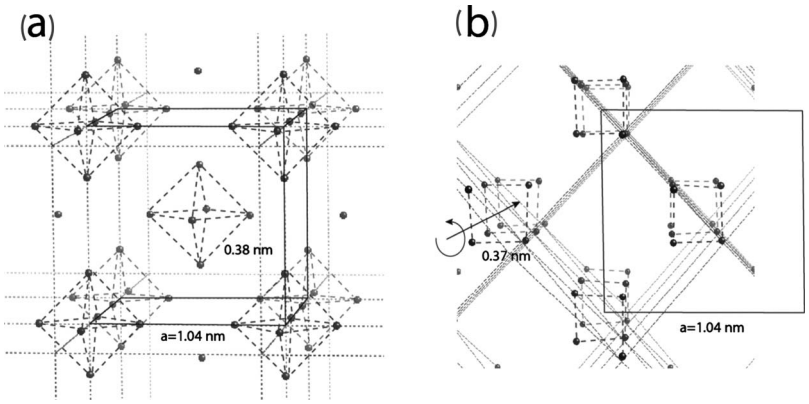

FIG. 5. Schematic drawing of the (a) I-centered and (b) 6010 structures as seen along a [001] direction of a Y cubic cell ($a=1.04$ nm for both structures); for clarity only hydrogen atoms on the octahedral sites are shown. (a) In the I-centered cubic structure the H_O atoms form vertex-connected octahedra centered at the Bravais lattice nodes; distances between the hydrogen atoms at the octahedral clusters are 0.38 nm. (b) In the 6010 structure the H_O atoms form spiral chains (with counterclockwise chirality shown with an arrow), with the distance between the H_O atoms of 0.37 nm.

Thus, for $x>0.0625$, all fcc-subsystem $Y_{fcc}H_{2+x}$ phases are metastable relative to $Y_{fcc}H_2+Y_{hcp}H_3$ at 0 K.

VI. COMPARISON OF EXPERIMENTAL AND COMPUTATIONAL RESULTS

The GS search for ordering in the mostly metastable $Y_{fcc}H_{2+x}$ solid solution predicts a number of ordered phases. As a screening procedure electron-diffraction patterns were calculated for the predicted fcc-GS structures [those with ΔE_f on the convex hull; Fig. 3(a)], the DO_{22}-type structure ($x=0.25$), and the I-centered cubic structure ($x=0.375$); all structures used for the calculations had fully relaxed atomic positions. The simulated electron-diffraction patterns for the [001]- and [110]-type orientations of an fcc-Y sublattice were compared with experimental SAED patterns. The simulated patterns were calculated using SINGLECRYSTAL™ software, with crystal thickness and intensity saturation kept constant for all diffraction patterns; the kinematic (single-scattering) approximation, which ignores dynamic electron scattering, was used.

Table II lists simulated structures and their [001]- and [110]-type patterns; the patterns' zone axes are indexed according to the corresponding Bravais lattices. Superlattice reflections of the simulated patterns are compared to the experimental patterns; patterns, which are close to the experimental, are labeled as "I" and those that differ are labeled with letters "A–D." From the experimental SAEDs the three ⟨100⟩ and six ⟨110⟩ patterns are equivalent. Thus, we conclude that only the I-centered ($x=0.375$) and 6010 structures ($x=0.0625$) fit the experiment.

Figure 4 shows the simulated [001]- and [110]-type patterns for the I-centered and 6010 structures. The patterns are very similar and resemble experimental patterns in Fig. 2 with the caveat that multiple scattering is ignored in the calculations and twinning is taken into account. Simulations of x-ray powder diffraction (XRD) from these structures yield practically indistinguishable patterns (dominated by scattering from Y). Simulated powder neutron diffraction exhibits some differences in the peak intensities of both fundamental and superlattice reflections. Simulations of phase contrast for the relaxed I-centered structure in [110] orientation reproduce the major feature of the experimental high-resolution images: enhanced intensity of spots along every fifth (110) plane. One such simulated image is shown as an inset in Fig. 1(b). Similar phase-contrast images were obtained for the relaxed 6010 structure.

Figure 5 shows drawings of these two structures projected along a [001] direction; for clarity only O-site hydrogen atoms, H_O, are shown. For the I-centered cubic structure [Fig. 5(a)], the H_O atoms form octahedra that are centered at the Bravais lattice nodes; distances between the hydrogen atoms in the octahedral clusters (octahedral edge lengths) are 0.38 nm.

In spite of the strong similarities of [001] diffractions in the 6010 and I-centered structures, their structural projections differ, such that all three ⟨001⟩ directions yield differently arranged (relative to their Y_{fcc} substructures) rows of H_O atoms. The square arrays of H_O atoms projected to ⟨100⟩ directions in 6010 as shown in Fig. 5(b) are actually projections of a spiral chain of H_O and V, with an H_O-H_O separation of 0.37 nm; corresponding projections in the I-centered cell are from square-planar arrays of H_O atoms. Intersections of the chains produce the projected squares in other cubic directions. In spite of its pseudocubic appearance and similarities in ⟨001⟩ projections, the 6010 structure is actually triclinic. It appears that only neutron diffraction can distinguish between the I-centered and 6010 structures.

Although the I-centered structure is not predicted to be a GS, even for the fcc-based $Y_{fcc}H_{2+x}$ subsystem, this does not preclude its (meta)stability at elevated temperature where it may be stabilized by configurational entropy from disorder on O sites and/or positional disorder within O sites. The O site is large for an H atom; hence, positional disorder within O sites is another possible source of entropy at elevated temperature. Investigation of the contribution from disorder requires a full first-principles phase diagram calculation, and the consideration of positional disorder within O sites is a much more difficult problem beyond the scope of this work. It is clear, however, that the fcc-based subsystem is more complicated than was portrayed in Ref. 21.

VII. CONCLUSIONS

Our experimental observations show the existence of long-range ordering in the fcc-based $Y_{fcc}H_{2+x}$ solid solution. From comparison of the experimental data and computational studies, two O-site-ordered structures with hydrogen fully occupying tetrahedral sites and ordered on octahedral sites are possible candidates: triclinic 6010 ($x=0.0625$) and I-centered cubic ($x=0.375$). It appears that the stable fcc-based ground-state phase $Y_{fcc}H_{2+x}$, in equilibrium with essentially stoichiometric $Y_{hcp}H_3$, has the 6010 $x=0.0625$ structure. Another candidate, the I-centered $x=0.375$ structure, is not ground state but may be stabilized by configurational entropy at above zero temperatures. The DO_{22}-type ordered structure is the only O-site ordered phase that has been reported in other rare-earth hydride systems.[8,29,30] Our calculations predict that it is a ground-state of the fcc-based subsystem that is metastable with respect to the $Y_{fcc}H_2+Y_{hcp}H_3$ two-phase mixture. Future work, such as neutron diffraction and first-principles phase diagram calculation, is necessary to determine the correct ordered structure of $Y_{fcc}H_{2+x}$.

[1] P. Vajda, in *Handbook on the Physics and Chemistry of Rare Earths*, edited by K. A. Gschneidner, Jr., and L. Eyring (North-Holland, Amsterdam, 1995), Vol. 20, p. 207.
[2] P. Vajda, Physica B **289-290**, 435 (2000).
[3] P. Vajda, Solid State Ionics **168**, 271 (2004).
[4] J. N. Huiberts, R. Griessen, J. H. Rector, J. P. Wijngaarden, D. G. deGroot, and N. J. Koeman, Nature (London) **380**, 231 (1996).
[5] R. Griessen, J. N. Huiberts, M. Kremers, A. T. M. van Gogh, N. J. Koeman, J. P. Dekker, and P. H. L. Notten, J. Alloys Compd. **253-254**, 44 (1997).

[6] P. Knappe, H. Muller, and H. W. Mayer, J. Less-Common Met. **95**, 323 (1983).
[7] T. J. Udovic, Q. Huang, and J. J. Rush, J. Alloys Compd. **356-357**, 41 (2003); T. J. Udovic, Q. Huang, A. Santoro, and J. J. Rush, Z. Kristallogr. **223**, 697 (2008).
[8] T. J. Udovic, J. J. Rush, Q. Huang, and I. S. Anderson, J. Alloys Compd. **253-254**, 241 (1997).
[9] A. K. Cheetham and B. E. F. Fender, J. Phys. C **5**, L35 (1972); C. G. Titcomb, A. K. Cheetham, and B. E. F. Fender, *ibid.* **7**, 2409 (1974).
[10] J. N. Huiberts, Ph.D. thesis, Free University, 1995.
[11] J. N. Daou and P. Vajda, Phys. Rev. B **50**, 012635 (1994).
[12] M. Kremers, N. J. Koeman, R. Griessen, P. H. L. Notten, R. Tolboom, P. J. Kelly, and P. A. Duine, Phys. Rev. B **57**, 4943 (1998).
[13] J. Schoenes, A. Borgschulte, A.-M. Carsteanu, H. Kierey, and M. Rode, J. Alloys Compd. **356-357**, 211 (2003).
[14] H. Kierey, M. Rode, A. Jacob, A. Borgschulte, and J. Schoenes, Phys. Rev. B **63**, 134109 (2001).
[15] A. Remhof, Ph.D. thesis, Fakultät für Physik und Astronomie an der Ruhr-Universität Bochum, 1999.
[16] J. R. Hattrick-Simpers, K. Wang, L. Cao, C. Chiu, E. Heilweil, R. G. Downing, and L. A. Bendersky, J. Alloys Compd. **490**, 42 (2010).
[17] E. J. Grier, K. Amanda, A. K. Petford-Long, and R. C. C. Ward, J. Appl. Crystallogr. **33**, 1246 (2000).
[18] E. J. Grier, O. Kolosov, A. K. Petford-Long, R. C. C. Ward, M. R. Wellsand, and B. Hjörvarsson, J. Phys. D **33**, 894 (2000).
[19] B. J. Kooi, E. Zoestbergen, J. T. M. deHossen, J. W. J. Kerssemakers, B. Dam, and R. C. C. Ward, J. Appl. Phys. **91**, 1901 (2002).
[20] K. Wang, J. R. Hattrick-Simpers, and L. A. Bendersky, Acta Mater. **58**, 2585 (2010).
[21] S. N. Sun, Y. Wang, and M. Y. Chou, Phys. Rev. B **49**, 6481 (1994).
[22] W. Wolf and P. Herzig, J. Alloys Compd. **356-357**, 73 (2003).
[23] G. Schöllhammer, W. Wolf, P. Herzig, K. Yvon, and P. Vajda, J. Alloys Compd. **480**, 111 (2009).
[24] J. Garcés, R. González, and P. Vajda, Phys. Rev. B **79**, 054113 (2009).
[25] G. Renaudin, K. Yvon, W. Wolf, and P. Herzig, J. Alloys Compd. **404-406**, 55 (2005).
[26] J. N. Daou and P. Vajda, Phys. Rev. B **45**, 10907 (1992).
[27] J. M. Sanchez, F. Ducastelle, and D. Gratias, Physica A **128**, 334 (1984).
[28] R. Kikuchi, Phys. Rev. **81**, 988 (1951).
[29] V. K. Fedotov, V. G. Fedotov, M. E. Kost, and E. G. Poniatovkii, Sov. Phys. Solid State **24**, 1252 (1982).
[30] G. André, O. Blaschko, W. Schwarz, J. N. Daou, and P. Vajda, Phys. Rev. B **46**, 8644 (1992).
[31] A. Remhof, G. Song, C. Sutter, D. Labergerie, M. Hubener, H. Zabel, and J. Hartwig, Phys. Rev. B **62**, 2164 (2000).
[32] D. G. Nagengast, J. W. J. Kerssemakers, A. T. M. van Gogh, B. Dam, and R. Griessen, Appl. Phys. Lett. **75**, 1724 (1999).
[33] A. van de Walle, M. Asta, and G. Ceder, Calphad **26**, 539 (2002).
[34] A. van de Walle and G. Ceder, J. Phase Equilib. **23**, 348 (2002).
[35] A. van de Walle and M. Asta, Modell. Simul. Mater. Sci. Eng. **10**, 521 (2002).
[36] A. van de Walle and G. Ceder, Rev. Mod. Phys. **74**, 11 (2002).
[37] G. Kresse and J. Hafner, Phys. Rev. B **47**, 558 (1993).
[38] G. Kresse, Ph.D Thesis, Technische Universitat Wien, 1993.
[39] G. Kresse and J. Hafner, Phys. Rev. B **49**, 14251 (1994).
[40] G. Kresse and J. Furthmuller, Comput. Mater. Sci. **6**, 15 (1996); Phys. Rev. B **54**, 11169 (1996); cf. http://tph.tuwien.ac.at/~vasp/guide/vasp.html
[41] H. T. Stokes and D. M. Hatch, J. Appl. Crystallogr. **38**, 237 (2005).